

www.acsami.org Research Article

# Tailoring Defects Regulation in Air-Fabricated CsPbl<sub>3</sub> for Efficient Inverted All-Inorganic Perovskite Solar Cells with $V_{\rm oc}$ of 1.225 V

Sheng Fu, Nannan Sun, Jiabo Le, Wenxiao Zhang, Renjie Miao, Wenjun Zhang, Yongbo Kuang, Weijie Song, and Junfeng Fang\*



Cite This: https://doi.org/10.1021/acsami.2c07420



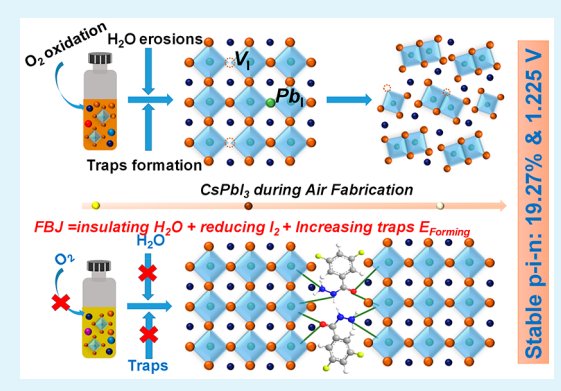
**ACCESS** 

Metrics & More

Article Recommendations

Supporting Information

ABSTRACT: Air fabrication of CsPbI $_3$  perovskite photovoltaics has been attractive and fast-moving owing to its compatibility to low-cost and upscalable fabrication. However, due to the inevitable erosions, undesirable traps are formed in air-fabricated CsPbI $_3$  crystals and seriously hinder photovoltaic performance with poor reproduction. Here, 3, 5-difluorobenzoic acid hydrazide (FBJ) is incorporated as trap regulation against external erosions in air-fabricated CsPbI $_3$ . Theoretical simulations reveal that FBJ molecules feature stronger absorbance on CsPbI $_3$  than water, which can regulate trap formations for water erosions. In addition, FBJ with solid bonding interaction to CsPbI $_3$  can enlarge formation energy of various defects during crystallization and further suppress traps. Moreover, profiling to reductive hydrazine groups, FBJ inhibits traps for oxidation erosions. Consequently, a champion efficiency of 19.27% with an impressive  $V_{\rm oc}$  of 1.225 V is realized with the inverted CsPbI $_3$  devices. Moreover, the optimized



devices present superior stability and contain 97.4% after operating at 60 °C for 600 h.

KEYWORDS: air fabrication, inverted inorganic perovskite photovoltaics,  $CsPbI_3$ , trap regulation,  $V_{oc}$  losses, stability

## 1. INTRODUCTION

Triiodide cesium lead (CsPbI<sub>3</sub>) perovskite with nonvolatile component and suitable bandgap has recently attracted extensive attention owing to their promising applications in both single-junction and tandem photovoltaics. 1-5 Despite high efficiency of 21% made on the regular (n-i-p) CsPbI<sub>3</sub> perovskite solar cells (PSCs),6 the fragile spiro-OMeTDA layers and the mismatched structure to the tandem devices are contrary to the future application of CsPbI3 photovoltaics. Inverted (p-i-n) CsPbI<sub>3</sub> PSCs can make up the shortcomings of the regular ones but are lagged. Along with the progress of efficiency, air fabrication of CsPbI3 has received wide attraction for future low cost and upscalable commercialization.<sup>6–11</sup> Massive attention is focused on the grains growth and intermediate phase control of the CsPbI3 films and promoted the progress of air-fabricated CsPbI<sub>3</sub> PSCs.<sup>6,7,11-14</sup> Apart from natural crystallization, the unavoidable external erosions of the water and oxygen would leave the damage marks on the CsPbI<sub>3</sub> films during their air fabrication. As proved by previous reports, surface iodine anions tend to escape from its initial lattices and dissolve into the water solvent when exposed to the humidity conditions 15-17 whereas oxygen can oxide the iodine anions into low-boil-point iodine (I<sub>2</sub>) and also cause the iodine losses in the air-fabricated CsPbI<sub>3</sub> PSCs. <sup>18–20</sup> The iodine-less components would result in the iodine vacancy (V<sub>I</sub>) traps and the lead-iodine antisite (Pb<sub>I</sub>) defect in the CsPbI<sub>3</sub> lattice. The

V<sub>I</sub> and Pb<sub>I</sub> traps would break up the balance between the neighboring [PbI<sub>6</sub>]<sup>4-</sup> octahedrons and would lower the freeenergy barrier for phase transition of CsPbI<sub>3</sub>. 17,21-24 In parallel, these traps can also act as nonradiative centers to capture carriers and hamper their  $V_{\rm oc}$  improvement. Furthermore, the crystallization of the CsPbI<sub>3</sub> has been proved to be significantly influenced by the humidity during air operation, 11,25 which leaves the limitation of air-fabricated CsPbI<sub>3</sub> PSCs. Molecular passivation has been widely used to regulate the crystallization and minimize the traps in the airfabricated CsPbI<sub>3</sub> films. 9,22-26 In particular, the organoamine halogen salts have played significant roles in the photovoltaic promotion of regular (n-i-p) CsPbI<sub>3</sub> PSCs as the surface termination, <sup>27–29</sup> additives, <sup>30,31</sup> and space cations of twodimensional CsPbI<sub>3</sub>. 32-34 Despite the considerable promotions for air-fabricated regulation with the organoamine halogen salts, comprehensively suppressing defects formation from the external erosions is still a challenge for air-fabricated CsPbI<sub>3</sub>

Received: April 27, 2022 Accepted: June 17, 2022



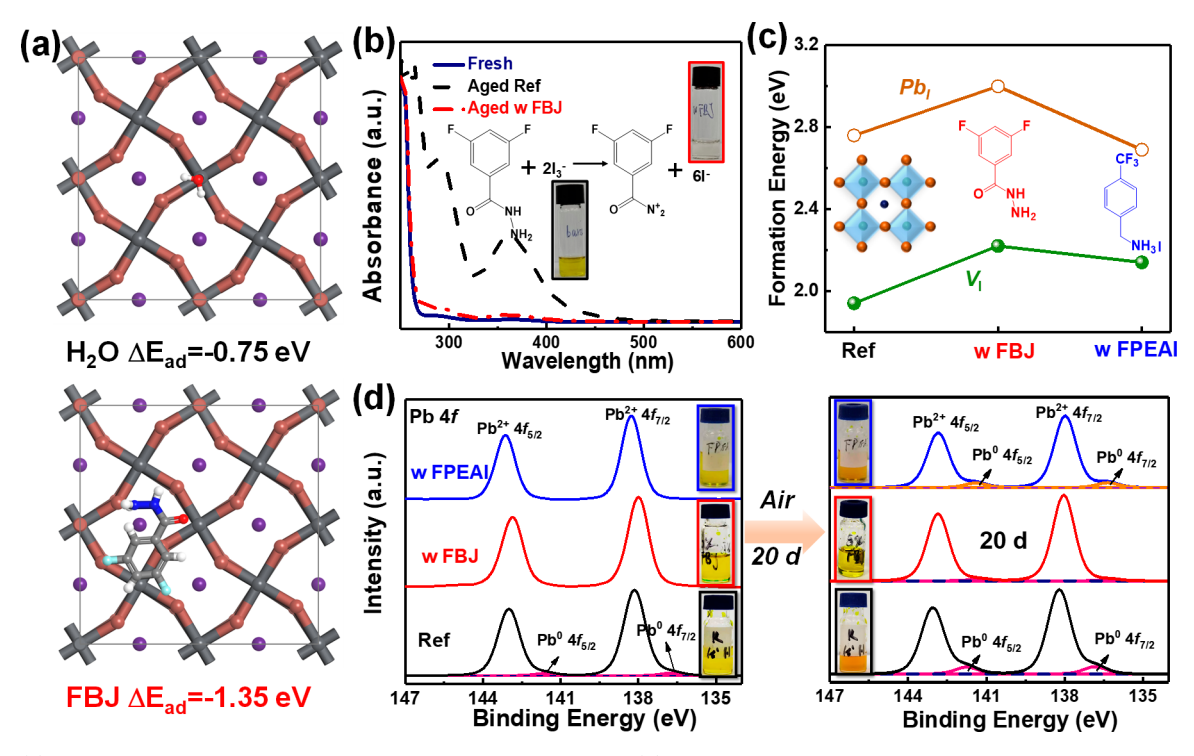


Figure 1. (a) Diagram of the DFT simulation with water and FBJ molecules. (b) UV—vis spectra of the different solutions, where the insets are the reaction equation and the photographs of the solutions. (c) Calculation results of the trap formation energies and the absorption energies with various molecules, where the insets are the molecular structures of various molecules. (d) XPS spectra of the CsPbI<sub>3</sub> films fabricated from the fresh and aged precursors.

films, which might also be of significance to the air-fabricated inverted structures.

Here, the 3, 5-difluorobenzoic acid hydrazide (FBJ) is chosen as the trap regulation for the air-fabricated CsPbI3 films for inverted inorganic perovskite photovoltaics. The FBI molecules have the stronger strength on the CsPbI3 surface than water (H<sub>2</sub>O), which could insulate the water erosion during air fabrication. Additionally, the reductive acylhydrazine groups can build the solid shield from the unideal precursor oxidation for oxygen erosions. Moreover, theoretical simulations point out that the FBJ molecules can strongly interact with CsPbI<sub>3</sub> components and enlarge the formation energies of the V<sub>I</sub> and Pb<sub>I</sub> defects. As a result, the FBJ molecules are more effective than the superstar passivator of p-trifluoromethylphenethylamine iodide (FPEAI) on trap regulation for airfabricated CsPbI<sub>3</sub> films. A champion efficiency of 19.27% with high  $V_{oc}$  of 1.225 V is realized based on inverted inorganic PSCs, which is also comparable to the regular devices (Table S1). Furthermore, the target devices present superior stability than incorporated FPEAI and the inverted device with FBJ remains 97.4% after maximum power output (MPP) tracking at 60 °C for 600 h.

#### 2. EXPERIMENTAL SECTION

**2.1. Materials and Precursor Solution Preparation.** The cesium iodide (CsI), lead iodide (PbI<sub>2</sub>), FPEAI, C60, and BCP were purchased from Xi'an Polymer Light Technology Corp. The dimethylammonium iodide (DMAI) and PCBM were offered by the Advanced Electionelection Technology Co., Ltd. The P3CT powders (Mw: 30–40K) was bought from the Rieke Metals. 3,5-Difluorobenzoic acid hydrazide (FBJ) was obtained from the Shanghai Macklin Biochemical Co., Ltd. All the raw materials are used without further treatment. The P3CT-N solution and PCBM (10 mg/mL in CB) were fabricated according to previous reports. <sup>16,25</sup>

The CsPbI $_3$  perovskite precursor was obtained by dissolving 0.65 M CsI (170 mg), 0.65 M PbI $_2$  (300 mg), and 0.78 M DMAI (135 mg) in 1 mL of DMF solvent. The concentrations of FBJ and FPEAI additives in precursor are 4 and 2 mg/mL, respectively.

**2.2. Devices Fabrication.** First, the patterned ITO substrates (2 × 2 cm<sup>2</sup>) were ultrasonically cleaned by detergent, deionized water, acetone, and isopropanol for 15 min, respectively. Before spin coating, the dried substrates were treated with the oxygen plasma for 5 min to increase the hydrophilicity. The P3CT-N hole-transport layers were coated at 4000 rpm for 30 s in ambient condition and annealed at 100 °C for 10 min. After cooling to room temperature, the substrates were preheated at 75 °C before coating. The CsPbI3 active layers were deposited by 2000 rpm for 25 s and then annealed at 200 °C for 8 min in controlled relative humidity (RH) 35% condition. After that, the CsPbI3 films were transported into a glovebox for 1,4butanediamine (DAB) surface treatment referring to previous reports<sup>35,36</sup> and PCBM deposition. Finally, the substrates were removed into the thermal evaporation equipment to deposit 20 nm C60, 8 nm BCP, and 130 nm silver (Ag) electrodes at the background vacuum of  $1.5 \times 10^{-4}$  Pa.

2.3. Characterizations and Stability Measurements. The XRD patterns of various films were collected by the Bruker AXS D8 Advance (Germany) equipped with Cu K $\alpha$  radiation ( $\lambda = 1.54$  Å). The crystalline morphology of different CsPbI<sub>3</sub> films was investigated by the field emission scanning electron microscope (SEM, Hitachi, S4800) at an accelerating voltage of 4 kV. The chemical environment changes after oxidation aging and FBJ incorporation and ultraviolet photoelectron spectroscopy (UPS) were estimated with the Kratos AXIS ULTRA. The photoluminescence properties were conducted by the Renishaw inVia Reflex and Delta Flex fluoroscence lifetime system (Horiba Scientific Cm., Japan) with excitation wavelength of 532 nm. The UV-vis absorption spectra were obtained with the model HP8453. The high-resolution transmission electron microscope (HR-TEM) images of FBJ doped films (16 mg/mL) were conducted the same way as in the literature.<sup>25</sup> SCLC curves were measured by the Keithley 2400 source meter. The capacitance-voltage (C-V) curves of various devices were collected at the electrochemical workstation.

The TPC and TPV measurements were obtained from the Zahner electrochemical workstation (Germany) at 80 mW/cm² lamp illumination. The photovoltaic performances of various inverted CsPbI $_3$  PSCs were obtained from the solar simulator (Newport Inc.) with an AM 1.5G filter. The EQE spectra were collected in glovebox with a Newport quantum efficiency measurement system (ORIEL IQE 200 TM). The phase stability of various films was conducted at controlled RH 35% drybox for 7 d. The moisture storage stability of the devices was estimated in a glovebox and controlled RH 10%. The  $J\!-\!V$  curves of the aged devices were obtained at regular time. The operational stability of the PSCs were measured by the PVLT-6001M-16A (Suzhou D&Rinstruments Co., Ltd.) under a 100 mW/cm² white LED array, and the environment temperature under illumination is around 60 °C. All the films and devices are aged without any encapsulation.

2.4. DFT Calculation Details. The DFT calculations were carried out using the freely available package, CP2K/Quickstep. The core electrons are represented by analytic Goedecker-Teter-Hutter (GTH) pseudopotentials.<sup>37</sup> The 1s electron of H, the 2s, 2p electrons of C, N, O, and F, 5s, 5p, 6s electrons of Cs, 5s, 5p electrons of I, and 6s, 6p electrons of Pb were treated as valence electrons.<sup>38</sup> The basis sets were double- $\zeta$  basis functions with one set of polarization functions (DZVP). The plane wave cutoff used for the density was 400 Ry. The wave function optimization was achieved using the orbital transformation (OT) minimizer with the convergence criteria  $1 \times 10^{-6}$  au. The PBE functional was used for all the calculation, and the Grimme D3 method was employed to correct the dispersion energy.  $^{39,40}$  The CsPbI<sub>3</sub>(100) surface was modeled by a 2  $\times$  2 supercell with four Pb-Cs layers, and considering it is a polar surface, the periodicity in the surface normal direction was removed. The adsorption energies ( $\Delta E_{ad}$ ) of FBJ, FPEAI, and H<sub>2</sub>O on the CsPbI<sub>3</sub> (100) surface were studied, and it was calculated by

$$\Delta E_{\rm ad} = E_{\rm S+ad} - E_{\rm S} - E_{\rm ad}$$

where  $E_{\text{S+ad}}$ ,  $E_{\text{S}}$ , and  $E_{\text{ad}}$  denote the total energies of the surface with adsorbed molecule, clean surface, and molecules, respectively. We also compared the formation energies of  $V_{\text{I}}$  and  $Pb_{\text{I}}$  on the clean CsPbI<sub>3</sub>(100) surface, FBJ adsorbed CsPbI<sub>3</sub>(100) surface, and FPEAI adsorbed CsPbI<sub>3</sub>(100) surface and considered all of the 16 I sites on the surface as the potential vacancy site. The formation energy ( $\Delta E_{\text{f}}$ ) of  $V_{\text{I}}$  and Pb<sub>I</sub> are calculated with

$$\Delta E_{\rm f} = E_{\rm S+V} - E_{\rm S} + \frac{1}{2} E_{\rm I_2}$$

and

$$\Delta E_{\rm f} = E_{\rm S+Pb} - E_{\rm S} + \frac{1}{2} E_{\rm I_2} - E_{\rm Pb}$$

where  $E_{S+V}$ ,  $E_{S+Pb}$ ,  $E_{I_2}$ , and  $E_{Pb}$  represent the total energies of the surface with a  $V_D$ , surface with a  $Pb_D$  iodine molecule, and Pb metal, respectively.

# 3. RESULTS AND DISCUSSION

Density functional theory (DFT) calculations are conducted to study the impact of the molecular construction on defects formation in CsPbI<sub>3</sub> (Figure S1). The Pb-rich CsPbI<sub>3</sub> (100) plane is considered as the exposed surface of CsPbI<sub>3</sub> because of its low surface energy (Figure S2a),  $^{22,41}$  and it is demonstrated that the FBJ molecule is anchored to the CsPbI<sub>3</sub> via the interaction between the hydrazide group and the surface Pb<sup>2+</sup>. First, we have calculated the adsorption strength of various molecules on the CsPbI<sub>3</sub>(100) surface (Figure 1a and Figure S2b) and found that the adsorption energies ( $\Delta E_{\rm ad}$ ) of FBJ, FPEAI, and H<sub>2</sub>O are following the order FBJ ( $-1.35~{\rm eV}$ ) < FPEAI ( $-1.22~{\rm eV}$ ) < H<sub>2</sub>O ( $-0.75~{\rm eV}$ ). It means the FBJ has more superior ability than FPEAI to prevent the CsPbI<sub>3</sub> from the water erosion during air fabrication. Another trap source

induced by the unideal oxidation reaction for the oxygen erosions also seriously hinders the progress of air-fabricated CsPbI<sub>3</sub> PSCs. As shown in Figure 1b, the DMAI solution has been oxidized into yellow with the absorbance peaks of I<sub>3</sub><sup>-</sup> anions in the UV-vis spectra after storage in air for 10 d. In sharp contrast, the FBJ incorporated solution remains colorless without obvious oxidation peaks within same operation. As proved by a previous report, 42 strongly reductive hydrazine groups can reduce the I2; thus FBJ can suppress the oxidation of iodides as the functions in Figure 1b inset and regulate trap formation from the oxygen erosions. Apart from the solid shields from external erosions, the strong interaction between CsPbI<sub>3</sub> and FBJ molecules may inhibit the components' escape and trap formations during the natural crystallization. Considering the iodine-less components for the oxygen and water erosion during air fabrication, the simulations of the formation energy of the V<sub>I</sub> and Pb<sub>I</sub> traps in the CsPbI<sub>3</sub> lattices are conducted with FPEAI and FBJ molecule absorption. It shows that the formation energies of the V<sub>I</sub> and Pb<sub>I</sub> on the FBJ adsorbed CsPbI<sub>3</sub> are 2.21 and 3.00 eV, respectively, and they are both larger than the formation energies of the V<sub>I</sub> and Pb<sub>I</sub> on the bare (Ref) and FPEAI adsorbed CsPbI<sub>3</sub> (Figure 1c). Thus, the construct with FBJ is the ideal trap regulation in the air-fabricated CsPbI3 films.

The Ref film fabricated from fresh precursor reveals the metal lead (Pb<sub>0</sub>) in the Pb 4f energy-level X-ray photoelectron spectroscopy (XPS) spectra (Figure 1d black line). Previous reports have proved that the Pb<sub>0</sub> signals in perovskite are mainly resulting from the V<sub>I</sub> traps and uncoordinated lead ions. 43,44 Without any protection, the humidity erosions would drive the iodine out of the films and leave the V<sub>I</sub> and Pb<sub>0</sub> traps in the lattices. In comparison, Pb<sub>0</sub> peaks are removed after incorporating the FBJ and FPEAI which directly support the humidity insulation and traps formation inhibition by molecular additives in the theoretic calculations. Additionally, the peaks of F 1s and N 1s energy-level signals emerge in the annealed films fabricated with FBJ and FPEAI incorporated precursor (Figure S3). The top-view energy dispersive X-ray (EDX) element mapping images of the FBJ incorporated (Figure S4) show uniform distribution of N and F elements, which reveals that nonvolatile FBJ molecules would gift the effective passivation and protection in CsPbI3 films. The HR-TEM image directly reveals the even distribution of FBJ molecules at GBs (Figure S5). In good agreement with the iodine anions' oxidation, the precursors of the Ref and FPEAI additive are gradually oxidized into brown color after 20 d of aging in air (Figure 1d inset), whereas the CsPbI<sub>3</sub> films deposited with the oxidized precursors reveal the obvious Pb<sub>0</sub> peaks even with FBJ incorporation (Figure 1d). In sharp contrast, the precursor with FBJ molecules remains with the unchanged color (light yellow) after the oxidation age, and the corresponding film shows inconsequential Pbo signals. Concurrently, the intensities of I 3d peaks in Ref and FPEAI doped films are gradually decreased with the precursor oxidation in air, while the FBJ incorporation reveals imperceptible change (Figure S6). The films fabricated from the oxidized precursors contain less iodine ions due to the volatile nature of I2 molecules, which further proves the existence of V<sub>I</sub> for oxidation. Thus, FBJ molecules are the tailored trap regulation to insulate the water and oxygen erosion for the air-fabricated CsPbI3 films.

All the CsPbI<sub>3</sub> films prepared with the different precursors show the similar  $\beta$  phase X-ray diffraction patterns (Figure 2a)

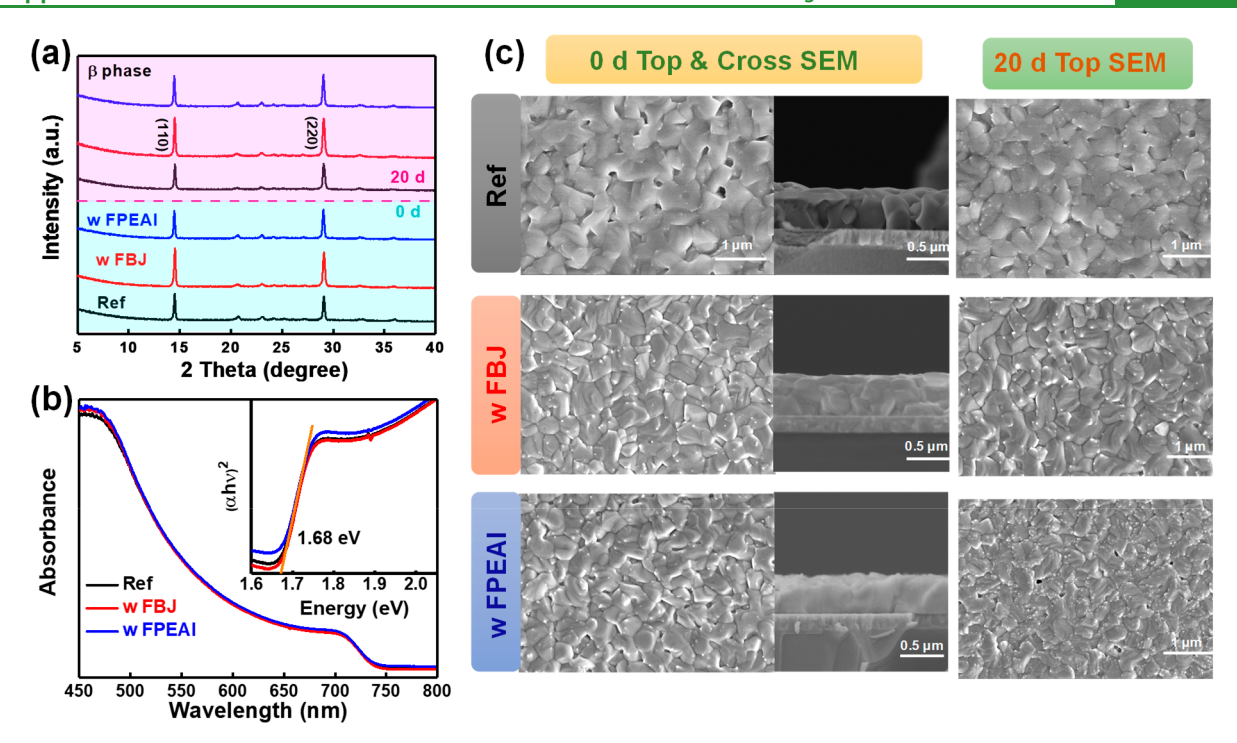


Figure 2. (a) XRD patterns of the  $CsPbI_3$  films fabricated from the aged precursors. (b) UV-vis absorption of various  $CsPbI_3$  films, where the inset figure is the Kubelka-Munk spectra calculated from the UV-vis absorption. (c) Top-view and cross-section SEM images of the Ref films, FBJ incorporated films, and FPEAI doped films fabricated from the fresh and aged precursors.

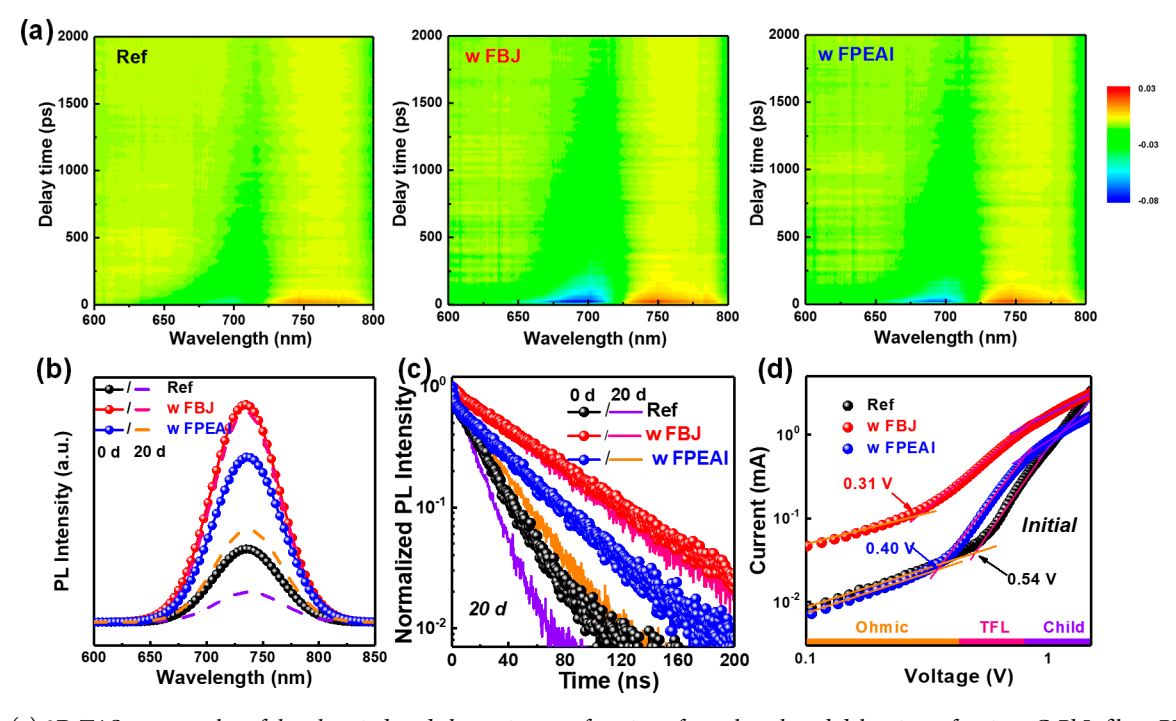


Figure 3. (a) 2D TAS contour plot of the photoinduced absorption as a function of wavelength and delay time of various CsPbI<sub>3</sub> films. PL (b) and TRPL (c) curves of the films fabricated from different precursors. (d) SCLC plots of the various CsPbI<sub>3</sub> films.

with optical bandgap of 1.68 eV (Figure 2b). The films fabricated from oxidized precursor reveal no impurity peaks or obvious intensity decrease in XRD patterns, suggesting that the precursor oxidation has the imperceptible phase change. When focusing on the diffraction intensity of each pattern, the FBJ doped films feature higher intensity than the Ref and FPEAI incorporated films. Focusing on the crystallization under low temperature (170 °C), the FBJ doped film presents a slower

color transition in comparison with the Ref (Figure S7). FBJ molecules with the carbonyl and hydrazine groups can strongly interact with the CsPbI<sub>3</sub> and control the growth for better crystallization. In good agreement, Ref films present inferior crystallization with nondense morphology in the scanning electronic microscope (SEM) images (Figure 2c), which might be attributed to the large nuclear energy of CsPbI<sub>3</sub>.<sup>45</sup> The FPEAI could ameliorate the crystallization, but the films also

**ACS Applied Materials & Interfaces** 

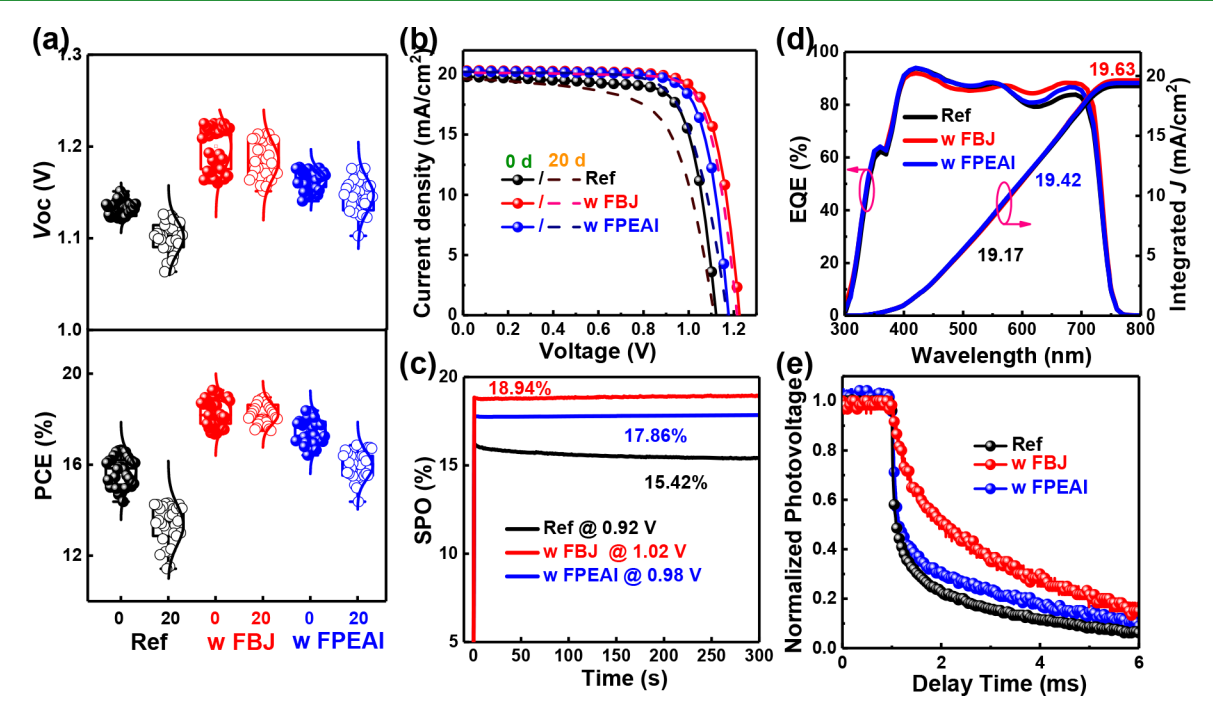


Figure 4. (a) Statistics of  $V_{oc}$  and FF parameters of various devices. (b-e) J-V curves (b), SPO curves (c), EQE spectra (d), and TPV measurements (e) of the champion efficiency of various devices.

feature some pinholes. In sharp contrast, FBJ incorporation could effectively remove the pinholes with dense morphology and enlarged grains, which would promote the optoelectronic properties of  $CsPbI_3$  films for less nonradiative recombination. The films fabricated from aged precursors present similar morphology with the fresh films, which indicates that the oxidation would not ruin the crystallization but leave massive  $V_{\rm I}$  in lattices.

To investigate the impact on the photogenerated carrier transfer dynamics of molecular constructions, we conduct ultrafast transient absorption spectroscopy (TAS) measurements on various films. As shown in Figure 3a, all the films present delay times over 2000 ps on the photoinduced absorption. The negative ground state bleaching band of the films is located at 700 nm, which originates from the fluorescence emission by edge recombination. In comparison, the FBJ doped film features slower decay than the Ref and FPEAI doped films (Figure S8), which indicates the lower recombination rate and less defects in the CsPbI3 films with FBJ incorporation. 46,47 In good agreement with the TAS results, the photoluminescence (PL) intensity of CsPbI<sub>3</sub> films is increased around triple fold after FBJ incorporation (Figure 3b) and the lifetime of the carriers (fitting from the timeresolved PL curves, Figure 3c and Table S2) is prolonged from the initial 16.69 to 49.36 ns with optimized concentration whereas the FBJ incorporation shows more promotion to the photoelectrical properties of CsPbI3 films than the FPEAI, corresponding to its effective defect regulation. The PL measurements are also performed on the films fabricated from the aged precursors. Both the PL intensity and carrier lifetime of Ref and FPEAI doped films are weakened by half after aging the precursors in air for 20 d. In sharp contrast, the target films deposited with the aged precursor display the ignorable changes on the PL performance, which directly demonstrates the inhibition of defects formation by FBJ molecules on precursor oxidation. We further conduct the

space charge limited current (SCLC) measurements with the hole-only structure to calculate the trap density  $(N_{\rm t})^{.48}$  As illuminated in Figure 3d (the fitting results in Table S2), the  $N_{\rm t}$  in CsPbI<sub>3</sub> films presents a significant reduction from the initial  $7\times 10^{15}~{\rm cm}^{-3}$  to  $4.02\times 10^{15}~{\rm and}~5.19\times 10^{15}~{\rm cm}^{-3}$  with FBJ and FPEAI incorporation, respectively. After the precursor oxidation ages, the  $N_{\rm t}$  of Ref and FPEAI doped films is enlarged (Figure S9), while the FBJ doped film presents little change. Both of the above phenomena point out that the FBJ molecules could regulate traps from defects formation and precursor oxidation for better optoelectronic properties in the air-fabricated films and thus would gift better photovoltaic performance to the inverted PSCs.

We also conduct ultraviolet photoelectron spectroscopy (UPS) on the various films to investigate the influence on energy levels of molecular construction (Figure S10a), and the calculated results are presented in Figure S10b. After molecular construction, the energy levels exhibit an upshift and the Femi energy  $(E_f)$  of the FBI doped features more n-type nature, which benefit the electron transfer between the CsPbI3 and PCBM layers. In addition, the energy level difference between the perovskite valence band maximum  $(E_v)$  and P3CT-N is minimized after FBJ and FPEAI incorporation, which can further reduce the  $V_{\rm oc}$  loss and gift the devices with higher build-in potential  $(V_{bi})$ . The  $V_{bi}$  of various devices are fitted from the capacitance-voltage (C-V) curves. The  $V_{\rm bi}$  is improved from initial 0.88 to 0.97 V after FPEAI incorporation, while a high  $V_{\rm bi}$  of 1.04 V is realized with FBJ employed (Figure S11). Thus, attributed to the less traps and matched energy levels after FBJ incorporation, the photovoltaic performance of air-fabricated inverted CsPbI<sub>3</sub> PSCs would get considerable improvement.

The PSCs with inverted structure of ITO/P3CT-N/CsPbI<sub>3</sub>/PCBM/C60/BCP/Ag are fabricated to estimate the influence of molecular construction on the photovoltaic performance (Figure S12). Thirty individual devices are taken into statistics

**ACS Applied Materials & Interfaces** 

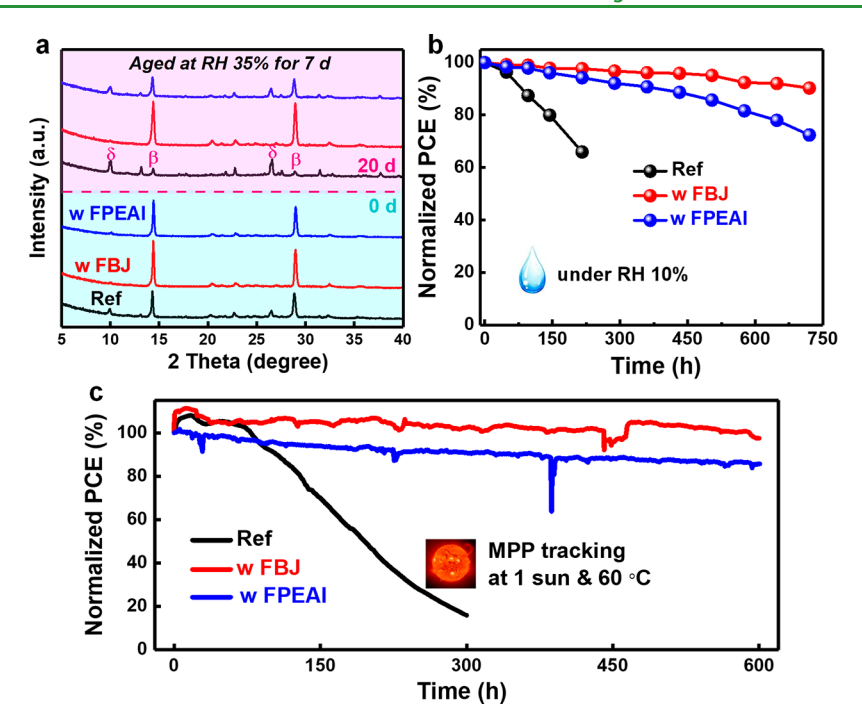


Figure 5. (a) XRD patterns various films after aging at RH 35% air for 7 d. Moisture stability under RH 10% (b) and MPP stability under 1 sun illuminated at 60  $^{\circ}$ C (c) of the devices fabricated from the fresh precursors.

for each condition, and the photovoltaic parameters are listed in the Table S3 and Figure 4a (other parameters are in Figure S13). The photovoltaic performances for optimization of dopants concentration are displayed in Table S4. Both the FBJ and FPEAI incorporations present the promotion of efficiency attributed to the higher  $V_{\rm oc}$  and filling factor (FF). And the precursor oxidation causes the poor reproducibility with reduction of  $V_{oc}$  and FF for the Ref and FPEAI devices, which originate from the serious nonradiative recombination for the oxidation-induced V<sub>I</sub> traps. In comparison, the devices fabricated from FBJ incorporated precursor still show good reproducibility even after exposure to air for 50 d (Figure S14). The I-V curves of the champion efficiency of various devices are displayed in Figure 4b. The Ref devices show a champion efficiency of 16.64% with a  $V_{\rm oc}$  of 1.121 V (decreased short power output (SPO) of 15.42%, Figure 4c) and reduction to 14.31% after precursor oxidation. The devices with FPEAI show a champion efficiency of 18.37% with high  $V_{\rm oc}$  of 1.176 V (stable SPO of 17.86%) and suffer from similar decrease (16.68%) to the Ref after oxidation. Significantly, the champion efficiency of the FBJ additive is 19.27% with  $V_{\rm oc}$ of 1.225 V, which is the highest  $V_{\rm oc}$  among CsPbI<sub>3</sub> PSCs, and the efficiency is comparable with the regular ones. Moreover, the optimized devices fabricated from the aged oxidized precursors maintain high efficiency of 18.93% with  $V_{\rm oc}$  of 1.214 V. In addition, profiling from the traps reduction and GBs passivation of FBJ incorporation, the hysteresis phenomenon is effectively suppressed (Figure S15), which could improve the operational stability of the inverted CsPbI<sub>3</sub> PSCs.

The current densities from the J-V curves of various devices are identified with the external quantum efficiency (EQE) spectra. The integrated current densities in the EQE spectra (Figure 3d) are 19.63, 19.42, and 19.17 mA/cm<sup>2</sup> for the devices with FBJ, with FPEAI and Ref, which are well matched with the measured  $J_{\rm sc}$ . Transient photocurrent (TPC) and transient photovoltage (TPV) measurements are performed to

investigate the carrier transport in the devices.  $^{49,50}$  Compared with the Ref and FPEAI doped devices, the target device reveals the slowest decay of photovoltage (Figure 4e) and shortest lifetime at the TPC measurements (Figure S16). Thus, it directly uncovers that the less nonradiative recombination and promoted carrier transports for FBJ incorporation are the origination of the superior photovoltaic performance with recorded  $V_{\rm oc}$ .

In addition to the limitation on photovoltaic performance, the traps in lattices would reduce the distortion energy of [PbI<sub>6</sub>]<sup>4-</sup> and accelerate the phase transition of CsPbI<sub>3</sub>.<sup>49</sup> First, we estimate the phase stability of the various films by aging at relative humidity (RH) 35% for 7 d. An undesirable  $\delta$  peak at 9.9° is in the XRD pattern of Ref films, while the FBJ and FPEAI doped films almost remain in the  $\beta$  phase (Figure 5a), corresponding to the phase stabilizing effects of the molecular construction. In comparison, the Ref and FPEAI doped films fabricated from the oxidation precursor have suffered from serious phase transition with obvious white regions in the XRD patterns and photographs (Figure S17) with in same operation whereas the precursor oxidation has no influence on the phase stability and the films with FBJ incorporation show good stability even when fabricated with the oxidized precursor. The worsening phase transitions of the Ref and FPEAI doped films with the oxidized precursor are mainly attributed to the oxidation-induced traps, which also emphasize the importance of inhibition defects from the formation and precursor oxidation for stable CsPbI3 PSCs. FBJ molecules can hinder the formation of V<sub>I</sub> and Pb<sub>I</sub> defects during air fabrication and fill the grains boundaries (GB) after annealing, which would prolong the duration of the PSCs. Our optimized device maintains almost the initial efficiency after storage in a glovebox for 60 d (Figure S18 and Table S5). In addition, corresponding to the humidity stability of the CsPbI3 films, the Ref device shows the rapid degradation to 65.92% of the initial efficiency after aging in RH 10% for 216 h, while the devices

with molecular constructions present the better humidity tolerance and the target device contains 90.28% after aging for 720 h (Figure 5b and the J-V curves in Figure S19). Operational stability under heating condition is the foundation of photovoltaic devices. However, the heat-sensitive doped spiro HTLs in the high-efficiency regular CsPbI<sub>3</sub> PSCs seriously hinder the thermal operational stability, 51,52 and the inverted structure would make up for this shortcoming. The operational stability of the nonencapsulation devices is investigated by MPP tracking at 60 °C with 1 sun illumination (Figure S20). The Ref device has lost the photovoltaic performance within 300 h of aging. In comparison, the device with FPEAI reveals the better operational stability and maintains 85.7% within the same tracking for 600 h (Figure 5c) whereas the FBJ doped device features the best duration and remained 97.47% (96.28% from the *J-V* measurements, Figure S21) of initial efficiency after 600 h tracking, which is superior to the reported CsPbI<sub>3</sub> PSCs. Our work has provided a new perspective on the molecular construction to regulate defects sources for high-performance CsPbI3-based optoelectronic devices.

#### 4. CONCLUSION

In summary, focusing on the defects formation for external erosions in the air-fabricated CsPbI3, we have tailored an effective regulator of FBJ for high-performance inverted PSCs. In comparison with the superstar passivator of FPEAI, the FBJ molecule with hydrazide groups can reduce the precursor oxidation for fewer traps. In parallel, the FBJ molecules feature stronger adsorption strength to the CsPbI3 than water and contain hydrophobic fluorine groups, which can inhibit the water-induced V<sub>I</sub> during air fabrication. Moreover, the strong interaction between the hydrazide groups and  $CsPbI_3$  can enlarge the defects formation energy in CsPbI<sub>3</sub> lattices. Consequently, a champion efficiency of 19.27% with high  $V_{\rm oc}$ of 1.225 V is realized based on the inverted CsPbI<sub>3</sub> PSCs, which is the highest  $V_{\rm oc}$  among the CsPbI<sub>3</sub> PSCs. The target devices also feature good reproduction against the precursor oxidation. Moreover, the devices with incorporated FBI present good stability against various ages and even remain 97.47% after MPP tracking at 60 °C for 600 h. Our work provides an excellent sight of trap regulation for highperformance inorganic perovskite optoelectronic devices.

## ASSOCIATED CONTENT

## Supporting Information

The Supporting Information is available free of charge at https://pubs.acs.org/doi/10.1021/acsami.2c07420.

EDXs, XPS spectra, HR-TEM image, C-V curves, UPS curves, summary table of the reported inverted inorganic PSCs, spectra, TPC measurements, photovoltaic performance, and stability characterization data (PDF)

## AUTHOR INFORMATION

### **Corresponding Authors**

Jiabo Le − Ningbo Institute of Materials Technology and Engineering, Chinese Academy of Sciences, Ningbo 315201, China; orcid.org/0000-0002-6570-5912; Email: lejiabo@nimte.ac.cn

Weijie Song – Ningbo Institute of Materials Technology and Engineering, Chinese Academy of Sciences, Ningbo 315201,

China; orcid.org/0000-0001-8129-8889; Email: weijiesong@nimte.ac.cn

Junfeng Fang — Ningbo Institute of Materials Technology and Engineering, Chinese Academy of Sciences, Ningbo 315201, China; School of Physics and Electronics Science, Engineering Research Center of Nanophotonics & Advanced Instrument, Ministry of Education, East China Normal University, Shanghai 200241, China; Center of Materials Science and Optoelectronics Engineering, University of Chinese Academy of Sciences, Beijing 100049, China; orcid.org/0000-0003-2094-8678; Email: jffang@phy.ecnu.edu.cn

#### **Authors**

Sheng Fu — Ningbo Institute of Materials Technology and Engineering, Chinese Academy of Sciences, Ningbo 315201, China; School of Physics and Electronics Science, Engineering Research Center of Nanophotonics & Advanced Instrument, Ministry of Education, East China Normal University, Shanghai 200241, China; Center of Materials Science and Optoelectronics Engineering, University of Chinese Academy of Sciences, Beijing 100049, China

Nannan Sun – Ningbo Institute of Materials Technology and Engineering, Chinese Academy of Sciences, Ningbo 315201, China; Center of Materials Science and Optoelectronics Engineering, University of Chinese Academy of Sciences, Beijing 100049, China

Wenxiao Zhang — School of Physics and Electronics Science, Engineering Research Center of Nanophotonics & Advanced Instrument, Ministry of Education, East China Normal University, Shanghai 200241, China

Renjie Miao – Ningbo Institute of Materials Technology and Engineering, Chinese Academy of Sciences, Ningbo 315201, China; Center of Materials Science and Optoelectronics Engineering, University of Chinese Academy of Sciences, Beijing 100049, China

Wenjun Zhang — Ningbo Institute of Materials Technology and Engineering, Chinese Academy of Sciences, Ningbo 315201, China; © orcid.org/0000-0001-6687-4091

Yongbo Kuang — Ningbo Institute of Materials Technology and Engineering, Chinese Academy of Sciences, Ningbo 315201, China; © orcid.org/0000-0002-0079-3720

Complete contact information is available at: https://pubs.acs.org/10.1021/acsami.2c07420

## **Author Contributions**

S.F. and N.S. contributed equally to this work.

#### Notes

The authors declare no competing financial interest.

#### ACKNOWLEDGMENTS

The authors thank the financial support of the National Natural Science Foundation of China (Grants 52173161, 61974150, 62104047, and 51773213), the Key Research Program of Frontier Sciences, CAS (Grant QYZDB-SSW-JSC047), Yongjiang Talent Introduction Programme (Grant 2021A-115-G), and the Fundamental Research Funds for the Central Universities (ECNU).

## REFERENCES

(1) Wang, Y.; Chen, Y.; Zhang, T.; Wang, X.; Zhao, Y. Chemically Stable Black Phase CsPbI<sub>3</sub> Inorganic Perovskites for High-Efficiency Photovoltaics. *Adv. Mater.* **2020**, *32*, No. e2001025.

- (2) Ho-Baillie, A.; Zhang, M.; Lau, C. F. J.; Ma, F.-J.; Huang, S. Untapped Potentials of Inorganic Metal Halide Perovskite Solar Cells. *Joule* **2019**, *3*, 938–955.
- (3) Tian, J.; Xue, Q.; Yao, Q.; Li, N.; Brabec, C. J.; Yip, H. L. Inorganic Halide Perovskite Solar Cells: Progress and Challenges. *Adv. Energy Mater.* **2020**, *10*, 2000183.
- (4) Steele, J. A.; Jin, H.; Dovgaliuk, I.; Berger, R. F.; Braeckevelt, T.; Yuan, H.; Martin, C.; Solano, E.; Lejaeghere, K.; Rogge, S. M. J.; et al. Thermal unequilibrium of strained black CsPbI<sub>3</sub> thin films. *Science* **2019**, 365, 679–684.
- (5) Zheng, X.; Alsalloum, A. Y.; Hou, Y.; Sargent, E. H.; Bakr, O. M. All-Perovskite Tandem Solar Cells: A Roadmap to Uniting High Efficiency with High Stability. *Acc. Mater. Res.* **2020**, *1*, 63–76.
- (6) Tan, S.; Yu, B.; Cui, Y.; Meng, F.; Huang, C.; Li, Y.; Chen, Z.; Wu, H.; Shi, J.; Luo, Y.; Li, D.; Meng, Q. Temperature-Reliable Low-Dimensional Perovskites Passivated Black-Phase CsPbI<sub>3</sub> toward Stable and Efficient Photovoltaics. *Angew. Chem., Int. Ed.* **2022**, No. e202201300.
- (7) Yu, B.; Shi, J.; Tan, S.; Cui, Y.; Zhao, W.; Wu, H.; Luo, Y.; Li, D.; Meng, Q. Efficient (>20%) and Stable All-Inorganic Cesium Lead Triiodide Solar Cell Enabled by Thiocyanate Molten Salts. *Angew. Chem., Int. Ed.* **2021**, *60*, 13436–13443.
- (8) Wang, X.; Wang, Y.; Chen, Y.; Liu, X.; Zhao, Y. Efficient and Stable CsPbI<sub>3</sub> Inorganic Perovskite Photovoltaics Enabled by Crystal Secondary Growth. *Adv. Mater.* **2021**, *33*, 2103688.
- (9) Chang, X.; Fang, J.; Fan, Y.; Luo, T.; Su, H.; Zhang, Y.; Lu, J.; Tsetseris, L.; Anthopoulos, T. D.; Liu, S. F.; Zhao, K. Printable CsPbI<sub>3</sub> Perovskite Solar Cells with PCE of 19% via an Additive Strategy. *Adv. Mater.* **2020**, 32, No. e2001243.
- (10) Fu, S.; Zhang, W.; Li, X.; Guan, J.; Song, W.; Fang, J. Humidity-Assisted Chlorination with Solid Protection Strategy for Efficient Air-Fabricated Inverted CsPbI<sub>3</sub> Perovskite Solar Cells. *ACS Energy Lett.* **2021**, *6*, 3661–3668.
- (11) Liang, L.; Li, Z.; Zhou, F.; Wang, Q.; Zhang, H.; Xu, Z.; Ding, L.; Liu, S.; Jin, Z. The humidity-insensitive fabrication of efficient  $CsPbI_3$  solar cells in ambient air. *J. Mater. Chem. A* **2019**, 7, 26776–26784.
- (12) Wang, P.; Zhang, X.; Zhou, Y.; Jiang, Q.; Ye, Q.; Chu, Z.; Li, X.; Yang, X.; Yin, Z.; You, J. Solvent-controlled growth of inorganic perovskite films in dry environment for efficient and stable solar cells. *Nat. Commun.* **2018**, *9* (1), 2225.
- (13) Zhang, J.; Fang, Y.; Zhao, W.; Han, R.; Wen, J.; Liu, S. Molten-Salt-Assisted CsPbI<sub>3</sub> Perovskite Crystallization for Nearly 20%-Efficiency Solar Cells. *Adv. Mater.* **2021**, *33*, 2103770.
- (14) Song, S.; Yang, S. J.; Choi, J.; Han, S. G.; Park, K.; Lee, H.; Min, J.; Ryu, S.; Cho, K. Surface Stabilization of a Formamidinium Perovskite Solar Cell Using Quaternary Ammonium Salt. *ACS Appl. Mater. Interfaces* **2021**, *13* (31), 37052–37062.
- (15) Lin, J.; Lai, M.; Dou, L.; Kley, C. S.; Chen, H.; Peng, F.; Sun, J.; Lu, D.; Hawks, S. A.; Xie, C.; et al. Thermochromic halide perovskite solar cells. *Nat. Mater.* **2018**, *17*, 261–267.
- (16) Fu, S.; Wan, L.; Zhang, W.; Li, X.; Song, W.; Fang, J. Tailoring In Situ Healing and Stabilizing Post-Treatment Agent for High-Performance Inverted CsPbI<sub>3</sub> Perovskite Solar Cells with Efficiency of 16.67%. ACS Energy Lett. 2020, 5, 3314–3321.
- (17) Xiang, W.; Liu, S.; Tress, W. A review on the stability of inorganic metal halide perovskites: challenges and opportunities for stable solar cells. *Energy Environ. Sci.* **2021**, *14*, 2090–2113.
- (18) Ke, F.; Wang, C.; Jia, C.; Wolf, N. R.; Yan, J.; Niu, S.; Devereaux, T. P.; Karunadasa, H. I.; Mao, W. L.; Lin, Y. Preserving a robust CsPbI<sub>3</sub> perovskite phase via pressure-directed octahedral tilt. *Nat. Commun.* **2021**, *12*, 461.
- (19) Chen, S.; Xiao, X.; Gu, H.; Huang, J. Iodine reduction for reproducible and high-performance perovskite solar cells and modules. *Sci. Adv.* **2021**, 7 (10), No. eabe8130.
- (20) Cho, J.; Kamat, P. V. How Chloride Suppresses Photoinduced Phase Segregation in Mixed Halide Perovskites. *Chem. Mater.* **2020**, 32 (14), 6206–6212.

- (21) Wang, L.; Zhou, H.; Hu, J.; Huang, B.; Sun, M.; Dong, B.; Zheng, G.; Huang, Y.; Chen, Y.; Li, L.; Xu, Z.; Li, N.; Liu, Z.; Chen, Q.; Sun, L.-D.; Yan, C.-H. Eu<sup>3+</sup>-Eu<sup>2+</sup> ion redox shuttle imparts operational durability to Pb-I perovskite solar cells. *Science* **2019**, *363*, 265–270.
- (22) Wang, H.; Bian, H.; Jin, Z.; Zhang, H.; Liang, L.; Wen, J.; Wang, Q.; Ding, L.; Liu, S. F. Cesium Lead Mixed-Halide Perovskites for Low-Energy Loss Solar Cells with Efficiency Beyond 17%. *Chem. Mater.* **2019**, *31* (16), 6231–6238.
- (23) Wu, T.; Wang, Y.; Dai, Z.; Cui, D.; Wang, T.; Meng, X.; Bi, E.; Yang, X.; Han, L. Efficient and Stable CsPbI<sub>3</sub> Solar Cells via Regulating Lattice Distortion with Surface Organic Terminal Groups. *Adv. Mater.* **2019**, *31*, No. e1900605.
- (24) He, J.; Liu, J.; Hou, Y.; Wang, Y.; Yang, S.; Yang, H. G. Surface chelation of cesium halide perovskite by dithiocarbamate for efficient and stable solar cells. *Nat. Commun.* **2020**, *11*, 4237.
- (25) Fu, S.; Li, X.; Wan, J.; Zhang, W.; Song, W.; Fang, J. In Situ Stabilized CsPbI<sub>3</sub> for Air-Fabricated Inverted Inorganic Perovskite Photovoltaics with Wide Humidity Operating Window. *Adv. Funct. Mater.* **2022**, 32 (14), 2111116.
- (26) Mahato, S.; Ghorai, A.; Srivastava, S. K.; Modak, M.; Singh, S.; Ray, S. K. Highly Air-Stable Single-Crystalline  $\beta$ -CsPbI<sub>3</sub> Nanorods: A Platform for Inverted Perovskite Solar Cells. *Adv. Energy Mater.* **2020**, 10 (30), 2001305.
- (27) Wang, Y.; Dar, M. I.; Ono, L. K.; Zhang, T.; Kan, M.; Li, Y.; Zhang, L.; Wang, X.; Yang, Y.; Gao, X.; Qi, Y.; Gratzel, M.; Zhao, Y. Thermodynamically stabilized beta-CsPbI<sub>3</sub>-based perovskite solar cells with efficiencies >18%. *Science* **2019**, *365*, 591–595.
- (28) Yang, S.; Wen, J.; Liu, Z.; Che, Y.; Xu, J.; Wang, J.; Xu, D.; Yuan, N.; Ding, J.; Duan, Y.; Liu, S. A Key 2D Intermediate Phase for Stable High-Efficiency CsPbI<sub>2</sub>Br Perovskite Solar Cells. *Adv. Energy Mater.* **2022**, *12* (2), 2103019.
- (29) Wang, X.; Ran, X.; Liu, X.; Gu, H.; Zuo, S.; Hui, W.; Lu, H.; Sun, B.; Gao, X.; Zhang, J.; Xia, Y.; Chen, Y.; Huang, W. Tailoring Component Interaction for Air-Processed Efficient and Stable All-Inorganic Perovskite Photovoltaic. *Angew. Chem., Int. Ed.* **2020**, 59 (32), 13354–13361.
- (30) Liu, T.; Zhang, J.; Qin, M.; Wu, X.; Li, F.; Lu, X.; Zhu, Z.; Jen, A. K. Y. Modifying Surface Termination of CsPbI<sub>3</sub> Grain Boundaries by 2D Perovskite Layer for Efficient and Stable Photovoltaics. *Adv. Funct. Mater.* **2021**, *31*, 2009515.
- (31) Kim, K. S.; Jin, I. S.; Park, S. H.; Lim, S. J.; Jung, J. W. Methylammonium Iodide-Mediated Controlled Crystal Growth of CsPbI<sub>2</sub>Br Films for Efficient and Stable All-Inorganic Perovskite Solar Cells. ACS Appl. Mater. Interfaces 2020, 12 (32), 36228–36236.
- (32) Jiang, Y.; Yuan, J.; Ni, Y.; Yang, J.; Wang, Y.; Jiu, T.; Yuan, M.; Chen, J. Reduced-Dimensional  $\alpha$ -CsPbX $_3$  Perovskites for Efficient and Stable Photovoltaics. *Joule* **2018**, *2*, 1356–1368.
- (33) Ye, Q.; Ma, F.; Zhao, Y.; Yu, S.; Chu, Z.; Gao, P.; Zhang, X.; You, J. Stabilizing gamma-CsPbI<sub>3</sub> Perovskite via Phenylethylammonium for Efficient Solar Cells with Open-Circuit Voltage over 1.3 V. *Small* **2020**, *16*, e2005246.
- (34) Sun, X.; Shao, Z.; Li, Z.; Liu, D.; Gao, C.; Chen, C.; Zhang, B.; Hao, L.; Zhao, Q.; Li, Y.; Wang, X.; Lu, Y.; Wang, X.; Cui, G.; Pang, S. Highly efficient  $CsPbI_3/Cs_{1-x}DMA_xPbI_3$  bulk heterojunction perovskite solar cell. *Joule* **2022**, *6* (4), 850–860.
- (35) Wu, W.-Q.; Yang, Z.; Rudd, P. N.; Shao, Y.; Dai, X.; Wei, H.; Zhao, J.; Fang, Y.; Wang, Q.; Liu, Y.; Deng, Y.; Xiao, X.; Feng, Y.; Huang, J. Bilateral alkylamine for suppressing charge recombination and improving stability in blade-coated perovskite solar cells. *Sci. Adv.* **2019**, 5 (3), eaav8925.
- (36) Khan, J.; Zhang, X.; Yuan, J.; Wang, Y.; Shi, G.; Patterson, R.; Shi, J.; Ling, X.; Hu, L.; Wu, T.; Dai, S.; Ma, W. Tuning the Surface-Passivating Ligand Anchoring Position Enables Phase Robustness in CsPbI<sub>3</sub> Perovskite Quantum Dot Solar Cells. *ACS Energy Lett.* **2020**, *5* (10), 3322–3329.
- (37) VandeVondele, J.; Krack, M.; Mohamed, F.; Parrinello, M.; Chassaing, T.; Hutter, J. Quickstep: Fast and accurate density

- functional calculations using a mixed Gaussian and plane waves approach. Comput. Phys. Commun. 2005, 167, 103-128.
- (38) Goedecker, S.; Teter, M.; Hutter, J. Separable dual-space Gaussian pseudopotentials. *Phys. Rev. B* **1996**, *54*, 1703–1710.
- (39) Perdew, J. P.; Burke, K.; Ernzerhof, M. Generalized Gradient Approximation Made Simple. *Phys. Rev. Lett.* **1996**, 77, 3865–3868.
- (40) Grimme, S.; Antony, J.; Ehrlich, S.; Krieg, H. A consistent and accurate ab initio parametrization of density functional dispersion correction (DFT-D) for the 94 elements H-Pu. *J. Chem. Phys.* **2010**, 132, 154104.
- (41) Gu, X.; Xiang, W.; Tian, Q.; Liu, S. Rational Surface-Defect Control via Designed Passivation for High-Efficiency Inorganic Perovskite Solar Cells. *Angew. Chem., Int. Ed.* **2021**, *60* (43), 23164–23170.
- (42) Wang, C.; Gu, F.; Zhao, Z.; Rao, H.; Qiu, Y.; Cai, Z.; Zhan, G.; Li, X.; Sun, B.; Yu, X.; Zhao, B.; Liu, Z.; Bian, Z.; Huang, C. Self-Repairing Tin-Based Perovskite Solar Cells with a Breakthrough Efficiency Over 11%. *Adv. Mater.* **2020**, 32, 1907623.
- (43) Li, F.; Deng, X.; Qi, F.; Li, Z.; Liu, D.; Shen, D.; Qin, M.; Wu, S.; Lin, F.; Jang, S.-H.; Zhang, J.; Lu, X.; Lei, D.; Lee, C.-S.; Zhu, Z.; Jen, A. K. Y. Regulating Surface Termination for Efficient Inverted Perovskite Solar Cells with Greater Than 23% Efficiency. *J. Am. Chem. Soc.* 2020, 142, 20134–20142.
- (44) Fu, S.; Li, X.; Wan, L.; Wu, Y.; Zhang, W.; Wang, Y.; Bao, Q.; Fang, J. Efficient Passivation with Lead Pyridine-2-Carboxylic for High-Performance and Stable Perovskite Solar Cells. *Adv. Energy Mater.* **2019**, *9*, 1901852.
- (45) Ma, J.; Qin, M.; Li, Y.; Wu, X.; Qin, Z.; Wu, Y.; Fang, G.; Lu, X. Unraveling the Impact of Halide Mixing on Crystallization and Phase Evolution in CsPbX<sub>3</sub> Perovskite Solar Cells. *Matter* **2021**, *4*, 313–327.
- (46) Gao, F.; Zhao, Y.; Zhang, X.; You, J. Recent Progresses on Defect Passivation toward Efficient Perovskite Solar Cells. *Adv. Energy Mater.* **2020**, *10* (13), 1902650.
- (47) Li, C.; Song, Z.; Chen, C.; Xiao, C.; Subedi, B.; Harvey, S. P.; Shrestha, N.; Subedi, K. K.; Chen, L.; Liu, D.; Li, Y.; Kim, Y.-W.; Jiang, C.-s.; Heben, M. J.; Zhao, D.; Ellingson, R. J.; Podraza, N. J.; Al-Jassim, M.; Yan, Y. Low-bandgap mixed tin-lead iodide perovskites with reduced methylammonium for simultaneous enhancement of solar cell efficiency and stability. *Nat. Energy* **2020**, *5*, 768–776.
- (48) Fu, S.; Zhang, W.; Li, X.; Wan, L.; Wu, Y.; Chen, L.; Liu, X.; Fang, J. Dual-Protection Strategy for High-Efficiency and Stable CsPbI<sub>2</sub>Br Inorganic Perovskite Solar Cells. *ACS Energy Lett.* **2020**, 5, 676–684.
- (49) Jiang, Q.; Zhao, Y.; Zhang, X.; Yang, X.; Chen, Y.; Chu, Z.; Ye, Q.; Li, X.; Yin, Z.; You, J. Surface passivation of perovskite film for efficient solar cells. *Nat. Photonics* **2019**, *13*, 460–466.
- (50) Yang, K.; Liao, Q.; Huang, J.; Zhang, Z.; Su, M.; Chen, Z.; Wu, Z.; Wang, D.; Lai, Z.; Woo, H. Y.; Cao, Y.; Gao, P.; Guo, X. Intramolecular Noncovalent Interaction-Enabled Dopant-Free Hole-Transporting Materials for High-Performance Inverted Perovskite Solar Cells. *Angew. Chem., Int. Ed.* **2021**, *61* (2), No. e202113749.
- (51) Jung, E. H.; Jeon, N. J.; Park, E. Y.; Moon, C. S.; Shin, T. J.; Yang, T. Y.; Noh, J. H.; Seo, J. Efficient, stable and scalable perovskite solar cells using poly(3-hexylthiophene). *Nature* **2019**, *567*, 511–515.
- (52) Arora, N.; Dar, M. I.; Hinderhofer, A.; Pellet, N.; Schreiber, F.; Zakeeruddin, S. M.; Gratzel, M. Perovskite solar cells with CuSCN hole extraction layers yield stabilized efficiencies greater than 20. *Science* 2017, 358 (6364), 768–771.

ī